Alloyed Copper Chalcogenide Nanoplatelets *via* Partial Cation Exchange Reactions

Vladimir Lesnyak,[†,*] Chandramohan George,[†,‡] Alessandro Genovese,[†] Mirko Prato,[†] Alberto Casu,[†] S. Ayyappan,[†] Alice Scarpellini,[†] and Liberato Manna[†]

[†]Department of Nanochemistry, Istituto Italiano di Tecnologia, via Morego, 30, 16163 Genova, Italy, and [‡]IFM-Department of Engineering, University of Cambridge, 17 Charles Babbage Road, Cambridge CB3 0FS, United Kingdom

ABSTRACT We report the synthesis of alloyed quaternary and quinary nanocrystals based on copper chalcogenides, namely, copper zinc selenide—sulfide (CZSeS), copper tin selenide—sulfide (CTSeS), and copper zinc tin selenide—sulfide (CZTSeS) nanoplatelets (NPLs) (∼20 nm wide) with tunable chemical composition. Our synthesis scheme consisted of two facile steps: *i.e.*, the preparation of copper selenide—sulfide ($Cu_{2-x}Se_yS_{1-y}$) platelet shaped nanocrystals *via* the colloidal route, followed by an *in situ* cation exchange reaction. During the latter step, the cation exchange proceeded through a partial replacement of copper ions by zinc or/and tin cations, yielding homogeneously alloyed nanocrystals with platelet shape. Overall, the chemical composition of the alloyed nanocrystals can easily be controlled by the amount of precursors that contain cations of interest (*e.g.*, Zn, Sn) to be incorporated/alloyed. We have also optimized the reaction conditions that allow a complete preservation of the size, morphology, and crystal structure as that of the starting $Cu_{2-x}Se_yS_{1-y}$ NPLs. The alloyed NPLs were characterized by optical spectroscopy (UV—vis—NIR) and cyclic voltammetry (CV), which demonstrated tunability of their light absorption characteristics as well as their electrochemical band gaps.

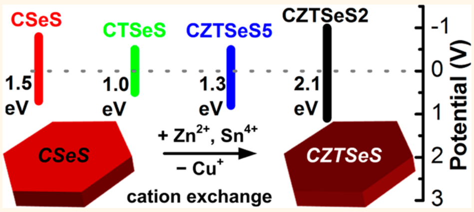

KEYWORDS: nanocrystals · copper chalcogenides · alloys · cation exchange · band gap engineering · cyclic voltammetry

During the last years, alloyed semiconductor nanomaterials based on copper chalcogenides have attracted significant interest owing to their potential in low-cost photovoltaic[1−14] and thermoelectric[15−21] applications. These materials are made up of elements such as Cu, Zn, S, and Se that are basically earth-abundant and relatively low-toxic. The first direct colloidal syntheses of quaternary Cu_2ZnSnS_4 (CZTS) nanocrystals (NCs) and their use in the fabrication of solar cells have been reported by Guo *et al.*,[2] and the Prieto[4] and the Korgel groups.[5] Thus, synthesized NCs can be used in the form of a concentrated ink, which is then cast into films *via* techniques such as drop-casting, dip- and spin-coating, spray deposition, inkjet printing, *etc.* Then, the deposited films are typically sintered to produce continuous and more compact films, as nearly as bulk material. To improve efficiency of the resulting solar cells, CZTS-films are often subjected to a selenization process (*i.e.*, annealing of the NC-substrates, typically at 500 °C under Se vapors),[2,3,9,11] which leads to grain growth, and the replacement of sulfur by selenium resulted in the narrowing of the materials band gap from 1.5 eV for CZTS to 1 eV as calculated for CZTSe.[22] On the other hand, compositionally tunable low-temperature photoluminescence of $Cu_2ZnSn(S_xSe_{1-x})_4$ NCs has recently been demonstrated by Singh *et al.*,[23] indicating their potential in photoemissive applications. Although even a multigram synthesis[24,25] and a continuous production[26] of CZTS nanoparticles in a flow reactor have already been developed, a significant control in terms of the size and shape is still not achievable by the direct synthesis for such complex quaternary materials, in contrast to well developed syntheses of binary semiconductor compounds (such as chalcogenides of zinc, cadmium, lead, mercury, as well as indium phosphide and arsenide). A few examples of the shape control in the colloidal synthesis of CZTS, reported to date, include wurtzite nanorods,[27] nanoprisms, and nanoplates.[28] As compared to CZTS,

* Address correspondence to vladimir.lesnyak@iit.it.

Received for review May 28, 2014 and accepted July 22, 2014.

10.1021/nn502906z

only a few synthetic approaches have so far been developed for CZTSe nanomaterials.[23,29−32]

Unlike the synthesis of binary compounds, the ternary and quaternary materials involve reactions between multiple precursors having different reactivities and, therefore, suffer from inherently poor control over NC nucleation and growth. This inevitably leads to broad variations in the size and, in some cases, in morphology and composition of the particles. This has been recently found by Ibáñez *et al.* in the synthesis of $Cu_2ZnGeSe_4$ NCs, where Cu_2Se nanoparticles were preferentially nucleated as the very initial step of the growth, followed by incorporation of Zn and Ge ions.[17] A similar mechanism has also been proposed by Shavel *et al.* for the growth of CZTS NCs starting with the nucleation of Cu_2S particles, followed by subsequent intercalation of Zn and Sn ions into the NC structure.[26] In such direct synthesis, the main drawback is that the incomplete conversion of Zn- and Sn-precursors into CZTSe NCs (30% of Sn and only 3% of Zn were incorporated)[29] leads to zinc- and/or tin-poor nonstoichiometric compounds,[33] which actually hinders the control on the composition of NCs. Additionally, in some cases, the particles exhibit an inhomogeneous distribution of elements, in particular Zn and Sn, over the quaternary NCs.[30] Therefore, apparently, the more complex the structure is, the more difficult it is to control its preparation. These issues clearly indicate that developing low-cost alloyed copper chalcogenides, such as CZTS, CZTSe, and CZTSSe, from more reliable synthetic routes, is of paramount importance for the future evolution of photovoltaics and thermoelectrics based on NCs.

Bearing in mind the discussions outlined above, here we report a straightforward and reproducible approach to prepare alloyed NCs, starting from a colloidal synthesis of $Cu_{2-x}Se_yS_{1-y}$ nanoplatelets (NPLs) employing a recently developed Se-precursor.[31] The nanoparticles thus obtained have been subjected to a partial cation exchange reaction based on the replacement of copper by zinc and/or tin ions in the copper selenide−sulfide crystal lattice, which has yielded CZSeS, CTSeS, and CZTSeS NPLs. In this way, our synthesis scheme combines a facile NC morphology control with its compositional tunability. As an additional advantage, cation exchange on already synthesized nanoparticles prevents possible separated nucleation events of corresponding binary and ternary compounds and ensures a homogeneous distribution of elements within the resulting alloy NCs. While complete cation exchange is a quite well developed method for the chemical transformation of binary NCs with preservation of their anion lattices *via* one-step or sequential exchange reactions, a partial exchange is an emerging technique which can yield a wide range of alloyed structures.[34−40] In our approach the composition of the particles is easily controllable by adjusting the initial feed ratio of Zn- and/or Sn-precursors to $Cu_{2-x}Se_yS_{1-y}$ NPLs in the reaction mixture, while preserving their size, shape and crystal structure. This variation of the composition allows for a precise tuning of the band gap of the obtained materials, as has been demonstrated by optical and cyclic voltammetry (CV) characterizations.

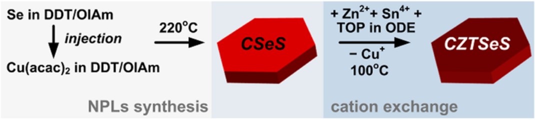

Figure 1. Scheme of the synthesis of pristine copper selenide−sulfide NPLs and subsequent cation exchange.

RESULTS AND DISCUSSION

As-synthesized copper selenide−sulfide platelet shaped NCs represent a convenient system for performing cation exchange reactions, given their large surface to volume ratio, as compared to spherical particles. Furthermore, 2D semiconductor crystals with a thickness smaller than their lateral dimensions are promising materials for micro- and optoelectronics.[41] The scheme of the NPLs synthesis with subsequent zinc and tin cations incorporation in the pristine NPLs is depicted in Figure 1. In a typical synthesis, the injection of the Se-precursor into the hot solution of Cu-precursor in 1-dodecanethiol (DDT)/oleylamine (OlAm) mixture yields NPLs with average lateral dimensions of 17.6 ± 4.6 nm and thickness of 4 ± 0.2 nm after 4 min of the reaction at 220 °C. The corresponding size distribution histogram of NPLs is presented in Figure SI1 (see the Supporting Information).

Conventional transmission electron microscopy (TEM) survey images display a view of the morphology and size distribution of as-synthesized NPLs (see Figure 2a). In particular, NPLs of similar sizes tend to spontaneously assemble into ribbons of face-to-face stacked platelets when they are deposited on TEM grids (see Figure SI2 in the Supporting Information), or in stacks made up of vertically arranged plates (see inset in Figure 2a). This stacking behavior is characteristic of the platelet shape and is often exploited for assembling CuS, Cu_2S, and $Cu_{2-x}Se$ nanodisks.[42−46] The atomic quantification of the pristine NPLs, obtained *via* energy dispersive X-ray spectroscopy (EDS), yielded content of Cu $65 \pm 1.3\%$, Se $26 \pm 1.1\%$, and S $9 \pm 0.7\%$, which corresponds to the composition $Cu_{1.82}Se_{0.74}S_{0.26}$ (see the inset in Figure 2d). We assume that incorporation of S into the NPLs occurs due to the DDT decomposition during the synthesis, similar to what has been found on copper selenide−sulfide and telluride−sulfide spherical particles,[47] as well as copper telluride NPLs.[48]

In spite of the similarity in the chemical composition of our platelets to that of pure $Cu_{2-x}Se$, their crystal structure was not compatible with cubic berzelianite. The corresponding powder X-ray diffraction (XRD)

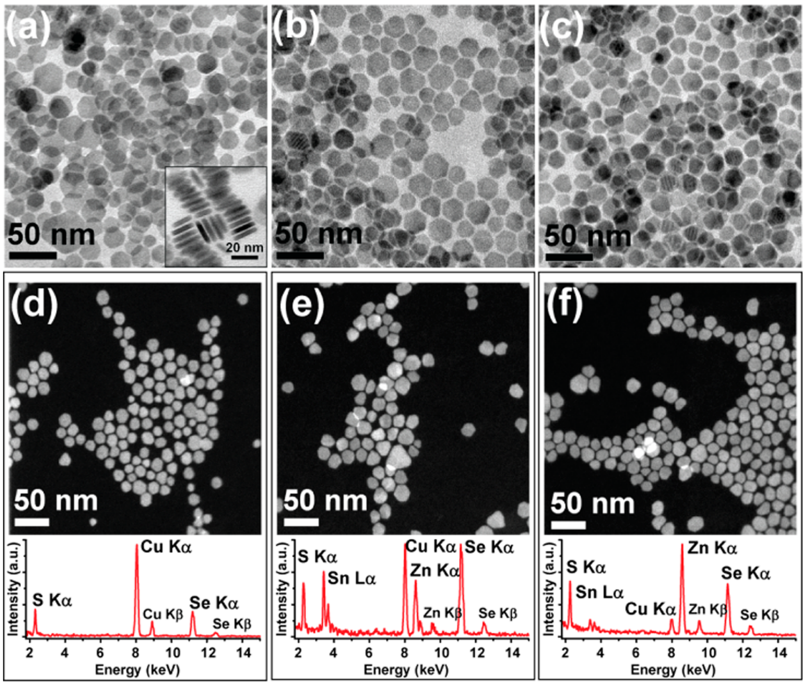

Figure 2. Conventional TEM images of pristine (a) and exchanged Cu-rich (CZTSeS5 in Table SI1 in the Supporting Information) (b) and Zn-rich (CZTSeS2) (c) NPLs. Inset in (a) shows corresponding NPLs arranged vertically. (d−f) High-angle annular dark field (HAADF) scanning TEM (STEM) observations of the NPLs shown in (a−c); insets below display their corresponding STEM-EDS spectra where the main peaks of S, Sn, Cu, Zn, and Se are shown consistent with chemical compositions of $Cu_{1.82}Se_{0.74}S_{0.26}$, $Cu_{0.54}Zn_{0.31}Sn_{0.23}Se_{0.79}S_{0.21}$, and $Cu_{0.15}Zn_{0.88}Sn_{0.04}Se_{0.75}S_{0.25}$ for the pristine, Cu-rich, and Zn-rich samples, respectively. Corresponding size distributions of the NPLs are shown in Figure SI1.

pattern can be indexed to two Cu_2S phases possessing a hexagonal sublattice of S atoms, *i.e.*, hexagonal high-chalcocite (JCPDS Card 84-0207) and monoclinic low-chalcocite (JCPDS Card 83-1462), as shown in Figure 3. Alternatively, it can be considered as a metastable phase with a hexagonal chalcocite-like structure,[49] in which ∼75% of the smaller S atoms in the anionic sublattice were substituted by larger Se atoms. A small deviation of the experimental diffraction pattern of pristine NPLs from the reference Cu_2S chalcocite phases should be ascribed to the different sizes of Se^{2-} and S^{2-} ions, leading to a volume dilation of the unit cell of the metastable chalcocite-like Cu−Se−S phase (see Figure 3a, lower inset). Such shift was recently observed by Singh *et al.* for CZTSSe NCs with varying their Se content from 0 to 1.[23] Crystal structure assessment of copper selenide−sulfide plates, performed *via* high resolution TEM (HR TEM), evidenced lattice sets and crystal axis directions compatible with hexagonal symmetry, confirming the XRD data. In particular, the main lattice sets displayed *d*-spacing of 2.0 and 3.6 Å with angular relationships consistent with {110} and {100} lattice planes of the hexagonal chalcocite-like structure (see Figure 3b).

As-prepared NPLs in the form of a crude reaction mixture were subjected to the cation exchange process, as depicted in the synthesis scheme in Figure 1. For the preparation of CZSeS and CTSeS alloys, cation precursors as zinc chloride ($ZnCl_2$) or tin(IV) bis(acetylacetonate) dichloride ($Sn(acac)_2Cl_2$) were employed. CZTSeS NPLs were synthesized *via* simultaneous reaction with both precursors at 100 °C in the presence of tri-*n*-octylphosphine (TOP), which, as a soft base, selectively binds to soft acid Cu^+ ions.[38,40] DDT and OlAm facilitate solubilization of zinc and tin salts *via* formation of metal−OlAm and metal−DDT complexes which react with the particles in a quite homogeneous system. Mild conditions of the cation exchange, such as moderate temperature and low concentrations of substituting ions, ensure complete preservation of the morphology of the initial NPLs (see Figure 2 and size distribution histograms in Figure SI1 in the Supporting Information). We note that at higher reaction temperatures (150−200 °C) etching of the plates occurred. As it was demonstrated by our group, the addition of a large excess of the Zn-precursor in the $Cu^+ \rightarrow Zn^{2+}$ exchange (typically Zn/Cu = 50−100/1) leads to a complete replacement of Cu ions.[49,50] Therefore, for a partial exchange, we have used precursors in molar ratios of Cu/Zn(Sn) $\leq$ 2. We have observed that the reaction of 2-fold molar excess of Zn-precursor relative to Cu led to approximately 85% replacement of copper ions with Zn^{2+} ions, yielding the ratio of Zn/Cu = 6 in the exchanged NPLs (see CZSeS sample in Table SI1 in the Supporting Information). As seen from the table, under the same synthetic conditions tin replaces only ∼30% of copper giving the final ratio Cu/Sn = 2.5 in the nanoparticles (CTSeS in Table SI1). Therefore, by addition of up to

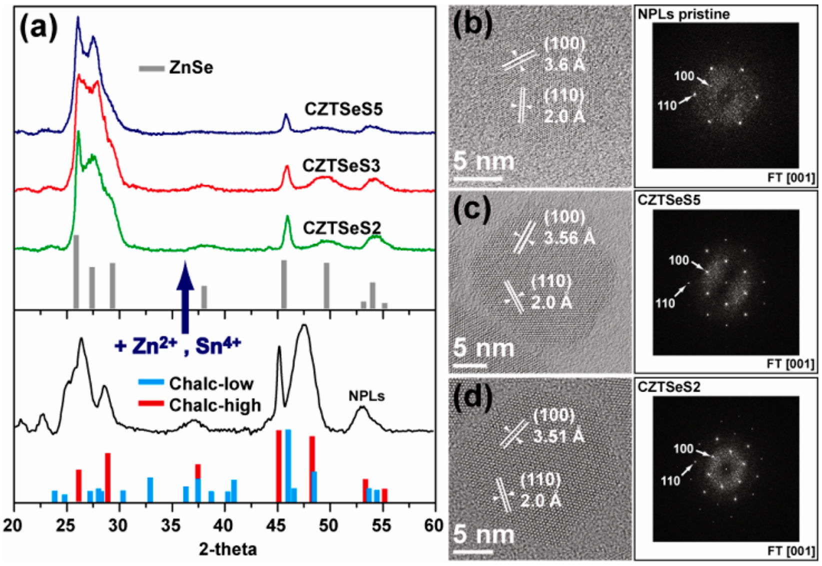

Figure 3. Structural characterization of NPLs. (a) XRD patterns of the pristine (lower inset), and the exchanged CZTSeS NPLs (for their compositions see Table SI1 in the Supporting Information) (upper inset). (b–d) HRTEM characterization of the corresponding NPLs displaying the main lattice sets {110} and {100} preserved before and after cation exchange, as confirmed by crystal axis angle relationship shown in the corresponding Fourier transform (FT) in the lateral insets.

2-fold excess of zinc- or tin-precursors, one can vary their incorporation level in the range of 0–85% for Zn and 0–30% for Sn, relative to copper in CZSeS and CTSeS particles, respectively.

When the two precursors are combined in one pot, it is possible to intercalate both Zn and Sn into $Cu_{2-x}Se_yS_{1-y}$ NPLs simultaneously. As follows from the data presented in Table SI1, by analogy with the separate cation exchange reactions, zinc is incorporated in a larger amount than tin. Limited incorporation of tin is probably due to a lower reactivity of the Sn-precursor, as compared to that of the Zn-precursor. In addition, Zn^{2+} has an ionic radius comparable to that of Cu^{+} ion (0.6 Å for both ions in the coordination number 4, and 0.74 and 0.77 Å for Zn^{2+} and Cu^{+} in the coordination number 6, respectively),[51] which should facilitate accommodation of zinc ions to the crystal lattice of copper sulfide–selenide. On the other hand, Sn^{4+} ions having smaller radius exhibit larger charge density that can hamper their diffusion within the crystals. Hence, zinc replaces Cu^{+} ions more efficiently, and since it is in a large excess, it can completely substitute them in Cu_2Se and Cu_2S NCs preserving their structure.[49,50] Therefore, to reach equivalent content of Zn and Sn in CZTSeS particles, the tin-precursor should be added in excess relative to zinc, as is demonstrated by the sample CZTSeS5. In this case, cation exchange reaction at the initial ratio of Cu/Zn/Sn = 8/1/4 yielded an alloy with a stoichiometry close to $Cu_2ZnSn(S,Se)_4$. The reaction with equal amounts of Zn and Sn with the same ratio between tin and copper (Cu/Sn = 2/1) led to a Zn-rich and Cu-, Sn-deficient composition (CZTSeS2). Here we note that Zn-rich and Cu-poor compositions of CZTS(Se) are known to provide higher efficiencies of solar cells built thereof.[9,12] Thus, by varying the content of the precursors in the cation exchange reaction, one can easily tune the composition of the resulting materials.

As revealed by TEM analysis, after the ion exchange reaction, a part of copper atoms located in cation sites was replaced by zinc or/and tin atoms. The incorporation of the guest ions tends to preserve the overall crystalline structure and morphological parameters of the NPLs, as shown by structural assessment performed *via* HRTEM and XRD analysis (see Figure 3), and by shape characterization performed *via* STEM imaging. The HRTEM crystal structure characterization and STEM-EDS chemical analysis of the exchanged NPLs were congruent with a direct incorporation process of Zn and Sn into the crystal lattice of the pristine platelets, thus giving rise to an alloy structure. No evidence of any anisotropic elements segregation/incorporation, such as reaction boundaries at the edges of particles, core/shell structures, janus-like structures or secondary phase nucleation, was observed. Moreover, all the area and point STEM-EDS analyses, carried out on a large number of single platelets, confirmed their alloy structure, as also established by STEM-EDS line mapping shown in Figure SI3 (see the Supporting Information).

The Se/S atom ratio in exchanged samples was practically the same as in the pristine plates (∼3/1), corroborating the preservation of the anionic sublattice.[49] The XRD characterization indicated that incorporation of zinc and tin cations into a chalcocite-like cell led to a slight rearrangement of the structure to hexagonal ZnSe (PDF card 01-080-0008). Thus, as seen in the upper inset of Figure 3a, the intensity of the main

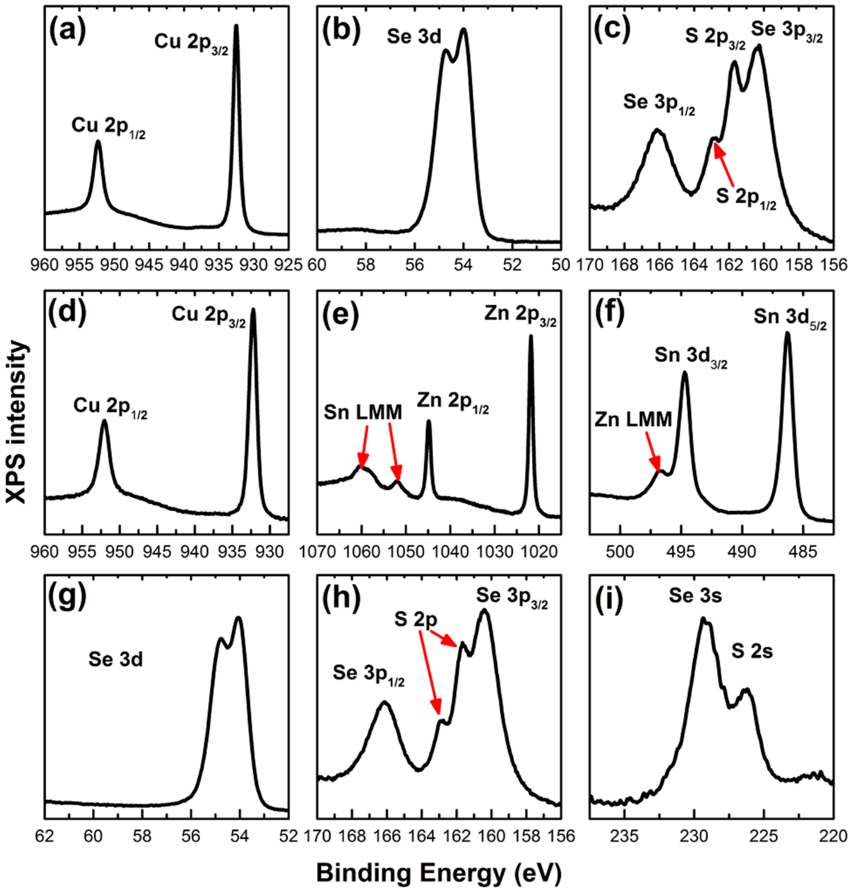

Figure 4. XPS narrow scans on Cu, Se, and S peaks of CSeS NPLs (a−c); Cu, Zn, Sn, Se, and S peaks of CZTSeS5 NPLs (d−i). Peak positions are listed in Table SI2 of the Supporting Information.

peaks increased and they became more prominent with increasing Zn content, *i.e.*, from CZTSeS5 to CZTSeS2. HRTEM measurements of CZTSeS NPLs revealed lattice sets with *d*-spacing of 2.0 and 3.5 Å and crystal axis relationships consistent with {110} and {100} lattice planes, given that the main hexagonal structure, imposed by anion hexagonal sublattice, was preserved during cation exchange (see Figure 3c,d). We believe that one of the factors responsible for the lattice preservation is DDT, which is known to help NCs of alloyed copper chalcogenides (such as CTSe,[52] CZTS,[27,28] and CZTSSe[23]) retain the wurtzite structure. It was demonstrated by Norako *et al*. that, without the addition of DDT, CTSe crystallizes in a phase-pure cubic product.[52]

To verify the phase-purity of the synthesized alloyed CZTSeS NPL compounds, we performed Raman spectroscopy measurements of CZTSeS2 and CZTSeS5 samples (for the spectra see Figure SI4 in the Supporting Information). From the best Lorentzian multiple peak fitting, the observed major peak positions at 196 and 330 cm^{-1} for Cu rich CZTSeS5 confirm the formation of alloy CZTSeS phase, which match well with the literature data.[23] In addition, the intensive Raman modes shift toward higher wave numbers by ~5 cm^{-1} for the Zn rich CZTSeS2 sample. In both cases Raman spectra clearly show single phase of CZTSeS without any impurities such as ZnS, ZnSe or initial CSeS seeds, which have strong vibrational modes at 351, 251, and 260 cm^{-1}, respectively.[53−56] Here we note that initial CSeS NPLs exhibited only a very weak Raman signal. Moreover, the absence of vibrational modes at 180 cm^{-1} further confirms the absence of CTSeS phase impurity.

X-ray photoelectron spectroscopy (XPS) analysis of the pristine and exchanged samples revealed that copper was present solely as Cu(I), since no Cu(II) satellites were observed (see Figure 4a,d). The shape of Se 3d peaks, shown in Figure 4b, suggests that NPLs contain mainly selenide ions (Se $3d_{5/2}$ line at 53.9 ± 0.2 eV), but also likely traces of di- or poly selenides.[57] The determination of the oxidation state of both zinc and tin requires XPS and Auger data, because the typical binding energy ranges for Zn(0)−Zn(II) pair, as well as for Sn(II)−Sn(IV) pair, overlap. In CZTSeS NPLs, zinc was present as Zn(II), according to the positions of its $2p_{3/2}$ and LMM peaks with binding energy of 1021.8 eV and kinetic energy of 989.9 eV, respectively (Figure 4e,f). For tin, we observed $3d_{5/2}$ peak at 486.3 eV, while the Sn MNN Auger peak is at approximately 434.6 eV of kinetic energy (Figure 4f,e). Since the reported position of the Auger peak for Sn(IV) species is always lower than 433 eV,[58] we could assign the oxidation state of tin as Sn(II). However, in this case, taking into account the

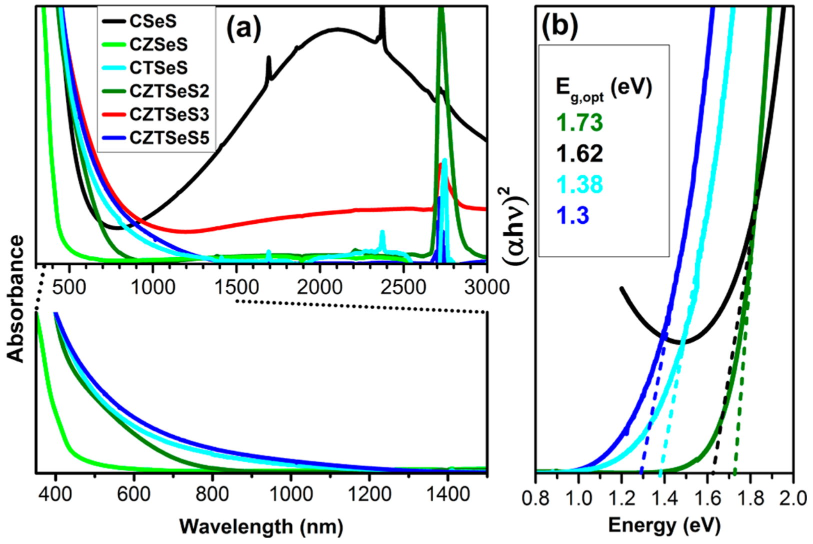

Figure 5. (a) Optical absorbance spectra of pristine $Cu_{2-x}Se_yS_{1-y}$, CZSeS, CTSeS, and CZTSeS NPLs obtained by the cation exchange (top). The corresponding zoomed region (350−1500 nm) without plasmonic samples is shown on the bottom. Note that sharp peaks in the NIR region arise from tetrachloroethylene and the traces of chloroform. (b) Corresponding plots of $(\alpha h\nu)^2$ *versus* energy with an extrapolation of the spectra (dashed lines) to determine optical band gap values of CSeS, CZTSeS2, CTSeS, and CZTSeS5 NPLs.

compositions of our alloyed compounds and the oxidation states of all constituting elements, we should note that we do not reach a proper balance between positive (metals) and negative (chalcogens) oxidation states. Therefore, our assignment of tin species as Sn(II) still needs a further clarification *via* alternative characterization techniques. A possible reducing agent for $Sn^{4+} \rightarrow Sn^{2+}$ reduction is DDT, which is present in a large amount, as compared to that of the cation precursor, in the reaction mixture. Analogous to the preparation of Se-precursor,[31] DDT can be easily oxidized forming disulfide. Related comparative studies on the cation exchange involving Sn^{2+} and Sn^{4+} precursors are currently ongoing in our group and will be published elsewhere. The oxidation state of Se did not change upon cation exchange, as shown in Figure 4g, where the Se 3d line is characterized by the same position and shape as in the case of pristine copper selenide−sulfide NPLs. The determination of sulfur oxidation is complicated due to the overlap with Se peaks, both for S 2p and S 2s lines (Figure 4h,i). However, the position of the main component of S 2p at 161.6 eV reveals the presence of sulfides S^{2-}.

We have observed by means of UV−vis-NIR spectroscopy that the incorporation of zinc and tin into $Cu_{2-x}Se_yS_{1-y}$ NPLs greatly alters their optical properties. As seen in Figure 5a, the pristine NPLs exhibit a broad localized surface plasmon resonance in the NIR region with maximum at ∼2100 nm, which is attributed to the oscillation of holes (Cu vacancies) created *via* oxidation processes[59−61] (we note that according to EDS analysis, $x = 0.18$ in as prepared copper selenide−sulfide particles). The broadening and red shift of the plasmon band, as compared to the commonly reported region of 1100−1300 nm[47,62−66] for $Cu_{2-x}Se$ and $Cu_{2-x}Se_yS_{1-y}$ NCs of various sizes and crystal structures, may be explained by considering such band as due to an "in-plane" resonance mode, analogous to that reported for CuS nanodisks.[67,68] This plasmon band is suppressed by the incorporation of guest cations into the copper selenide−sulfide structure, which in turn could fill copper vacancies and, if needed for the charge compensation, extract electrons from the environment. Interestingly, a sample with a high Zn content, equal to Cu (CZTSeS3 in Table SI1 of the Supporting Information, Cu/Zn = 1/1), still exhibits a broad plasmon band of low intensity (see Figure 5a), revealing the presence of copper vacancies in the alloyed lattice. Even the sample with dominating ZnSe crystal structure (CZSeS) has a very weak absorption in the NIR region. Upon increasing tin content (see samples CZTSeS3−5 in Figure SI5 of the Supporting Information), the plasmon was dampened and the absorption onset was shifted toward longer wavelengths, most likely due to the removal of the Cu vacancies, which lowers the free carrier (hole) density.

The addition of cerium(IV) ammonium nitrate $(NH_4)_2Ce(NO_3)_6$ used as an oxidizing agent[47,62] to these samples did not lead to the appearance of the plasmon band (*i.e.*, Cu-vacancies were not generated), confirming their stability against oxidation (see Figure SI6 in the Supporting Information). As seen from the spectra in Figure 5a, the farthest IR absorbers among the nonplasmonic samples synthesized contain the largest amount of tin (CTSeS and CZTSeS5, with absorption onset at ∼1350−1400 nm), suggesting that they have the narrowest band gaps, as confirmed by estimation of their optical band gaps presented in Figure 5b.

The direct optical band gaps ($E_{g,opt}$) of pristine CSeS, as well as exchanged CZTSeS2, CTSeS, and CZTSeS5 NPLs were determined from their absorbance spectra by extrapolation of the linear region of $(\alpha h\nu)^2$ plots *versus* energy, where α is a corresponding absorption and $h\nu$ is the photon energy. In general, all the alloy NPLs synthesized in this work exhibit featureless bulk-like absorption profiles which are characteristic of CTSe and CZTS(Se) nanomaterials reported to date.[2,23,27,29,52,69]

To investigate the electrochemical behavior of the synthesized NPLs, which is particularly important for their application as light absorbers in solar cells, we have performed cyclic voltammetry (CV) measurements. In general, CV has been proven as an effective technique for the characterization of semiconductors in determining their electrochemical band gaps ($E_{g,EC}$) as well as the energy levels of the highest occupied molecular orbital (HOMO) and the lowest unoccupied molecular orbital (LUMO). Conventionally, materials such as conjugated polymers have been investigated by CV in order to assess their energy levels and $E_{g,EC}$,[70] since the onset of red-ox currents (in CV traces) can be correlated to the electron affinity (E_a) and ionization potential (I_p) according to the calculations performed by Bredas *et al.*[71] Subsequently, this method has increasingly been used to assess the electrochemical properties and $E_{g,EC}$ of semiconductor NCs,[72] such as CdSe, CdTe, $CdSe_xTe_{1-x}$,[73] and CdS_xSe_{1-x}.[74] Recently, materials such as Cu chalcogenide-based NCs have also been investigated *via* CV. For example, Ahmadi *et al.* reported the $E_{g,EC}$ of ~20 nm sized Cu_2SnSe_3 NCs to be 1.5 eV, which was however slightly higher than the optically determined band gap value $E_{g,opt}$ = 1.3 eV.[75] Furthermore, chalcopyrite type $CuInS_2$ NCs with size ranges of 3−8 nm have been characterized by size-dependent $E_{g,EC}$ values.[76]

In typical CV measurements the potentials at which the red-ox (reduction/oxidation) processes take place are commonly referenced to the standard hydrogen electrode potential (NHE) for estimating the $E_{g,EC}$ of NCs.[77] The positions of energy levels of nanocrystalline materials can be clearly resolved as red-ox peak onsets representing their HOMO/LUMO states. This means that the electron transfer process (*i.e.*, withdrawing or injecting electrons) is mediated through the valence band (VB) edge and conduction band (CB)[74] edge for a given semiconductor NC. Copper chalcogenides such as $Cu_{2-x}S$, $Cu_{2-x}Se$ and $Cu_{2-x}S_ySe_{1-y}$, which are characterized by large free carrier densities, display $E_{g,opt}$ values in the range of 1.2−2 eV[78] and also exhibit clear red-ox processes involving charge transfer.[79] In our electrochemical measurements, the as-prepared NPLs (without any surface treatment) were directly deposited onto glassy carbon electrodes, and thoroughly dried in order to obtain NPL films. In the CV traces presented in Figure 6a, the NPLs had evidenced prominent and asymmetric peaks related to their oxidation and reduction processes separated by a gap in terms of the potentials (V). This is indicative of an energy barrier or gap between the band edges of the NPLs. Here, the oxidation current can be related to the addition of holes to the HOMO level, while the reduction is related to the addition of electrons to the LUMO of NPLs, which are directly derivable from the onset of anodic and cathodic currents in CV traces. Therefore, the onset points, from which the prominent current peaks had emerged along the potential scan, have been deduced (as indicated in Figure 6a). These onset points can also be used to identify the positions of VB and CB edges of the NPLs, upon adding/removing electrons, according to the equations $E_a(E_{LUMO}) = -(E_{pc}{}^{red} + 4.4)$ eV; $I_p(E_{HOMO}) = -(E_{pa}{}^{ox} + 4.4)$ eV, where $E_{pc}{}^{red}$ and $E_{pa}{}^{ox}$ are the onsets of reduction and oxidation potentials, as discussed earlier. After a gap (where there was no flow of an appreciable current) along the potential scan, these points of current onsets led to multiple peaks in both oxidation and reduction potentials, which were typically in the range of approximately −1.0 to −0.3 V for reduction and +1.7 to +0.5 V for oxidation, as indicated in Figure 6a. From these onsets, the corresponding $E_{g,EC}$ values were deduced. They are reported in Figure 6b, and plotted with reference to TiO_2 band positions,[80] which is most commonly employed as a transparent electron-accepting layer in heterojunction solar cells.[81−85] The appearance of additional peaks in the CV traces is typical for semiconductor nanomaterials, and they are often related to different surface states[86] since a CV scan is extremely

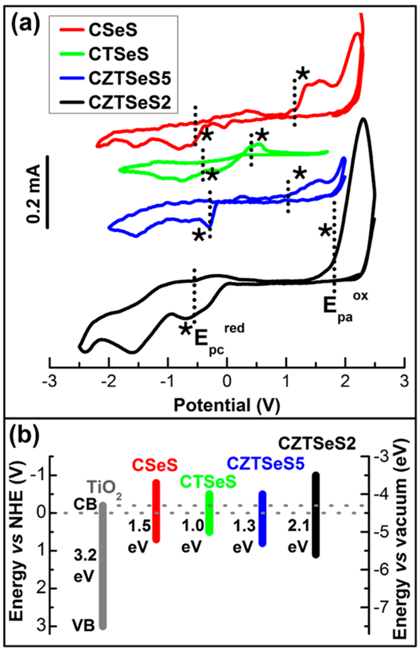

Figure 6. CV responses of pristine CSeS, CTSeS, and CZTSeS NPLs obtained by the cation exchange (a). The band gap positions of the materials synthesized with respect to the conduction and valence band levels of TiO_2[80] with energies reported *vs* NHE and vacuum (b).

sensitive to the presence of defects that, for example, could activate trap states in NPLs. Nevertheless, a general consensus is that the band gaps ($E_{g,EC}$) calculated *via* CV is slightly higher than the optically measured ones ($E_{g,opt}$).[70,72] For instance, as follows from comparison of Figures 5b and 6b, the estimated $E_{g,EC}$ values for CSeS and CZTSeS5 NPLs were much closer to the optically estimated $E_{g,opt}$ ones, while the samples CTSeS and CZTSeS2 exhibited larger differences. This is partly because the zinc incorporation in these crystals increases their red-ox energies due to the widening of their band gap. In our case, the reported $E_{g,EC}$ for various types of NCs developed can have a maximum difference of ±0.25 eV.

As displayed in Figure 6b, $E_{g,EC}$ of the investigated NPLs ranges from 1.0 to 2.1 eV. From the data presented, one can observe a good correlation between the different compositions of NPLs and their corresponding band gap values. Thus, for instance, the composition of CZTSeS2 with the highest Zn content and the lowest Sn content is reflected in a wide band gap (2.1 eV), which narrows down with reducing Zn and increasing Sn amount (1.3 eV for CZTSeS5). Incorporation of solely tin ions into $Cu_{2-x}Se_yS_{1-y}$ NPLs also results in a narrowing of their band gap from 1.5 to 1.0 eV. Additional verification of our band gap estimation provides a comparison with recently published data on CZTSeS NCs with composition similar to our CZTSeS5 sample. Thus, the band gap of CZTSeS was evaluated as 1.19 eV, both optically and electrochemically, with its CB and VB edges at −4.53 and −5.72 eV, respectively.[87] The difference between these data and our results ($E_g = 1.3$ eV; CB and VB edges = −4.0 and −5.3 eV, respectively) can be explained by differences in the NC composition, *i.e.*, higher Cu and Zn, and lower Sn contents ($Cu_{2.15}Zn_{1.24}Sn_{0.92}Se_{3.2}S_{0.8}$ *vs* reported $Cu_2ZnSnSe_{3.2}S_{0.8}$).

Overall, as seen in Figure 6b, the calculated band edges of the samples lie above the CB edge of TiO_2 (as well as ZnO[80]) suggesting that they are suitable as light absorbers for heterojunction solar cells. Among them, CTSeS and CZTSeS5, which possess narrowest band gaps with CB edges situated 0.3 eV above that of TiO_2, that should prevent the back transport of electrons, and which, at the same time, exhibit light absorption extended to the NIR region (see Figure 5) are the most promising candidates for photovoltaic applications. In addition, a large discontinuity between their HOMO levels and that of titanium oxide (>1 eV) should, in principle, prevent hole transfer and charge recombination at the NPLs/TiO_2 interface.

CONCLUSION

We have developed a convenient approach for the preparation of copper zinc (tin) selenide−sulfide (CZSeS and CTSeS) and copper zinc tin selenide−sulfide (CZTSeS) nanoplates (~20 nm) with tunable band gap. Our synthesis scheme essentially involves a combination of colloidal synthesis for the starting $Cu_{2-x}Se_yS_{1-y}$ NPLs and an *in situ* partial cation exchange for alloying. Remarkably, the initial feed ratio of cation precursors (*i.e.*, Zn and/or Sn) to copper ions appears to mediate the final composition of the alloyed compounds without altering the morphology and hexagonal crystal structure as that of the starting copper selenide−sulfide NPLs. The strategy proposed by us can be extended to other cations, as well as other copper chalcogenide nanoparticles, *i.e.* copper sulfide and telluride, with various shapes and crystal structures, or to design new chemical compounds with metastable crystal phases yielding more complex tailor-made nanomaterials with tunable properties, which otherwise would be more difficult to access from the direct synthesis. We demonstrate that by the incorporation of guest zinc and tin cations into Se/S anion framework of $Cu_{2-x}Se_yS_{1-y}$ NPLs, it is possible to engineer the band gap of the resulting alloyed NCs, which opens new opportunities for their application as light absorbers to fabricate solar cells.

METHODS

Materials. Copper(II) acetylacetonate ($Cu(acac)_2$, 97%), $ZnCl_2$ (99.999%), $Sn(acac)_2Cl_2$ (98%), DDT (≥98%), OlAm (70%), 1-octadecene (ODE, 90%), tetrabutylammonium perchlorate (TBAP, ≥98%), acetonitrile (99.8%), tetrachloroethylene (TCE, ≥99%), acetone (≥99.5%), and dichloromethane (≥99.8%) were purchased from Sigma-Aldrich; selenium powder (Se, 99.99%), TOP (97%) were from STREM chemicals; chloroform (anhydrous, 99.95%), methanol (anhydrous, 99.9%) were from Carlo Erba reagents. All chemicals were used as received without further purification.

Synthesis of $Cu_{2-x}Se_yS_{1-y}$ NPLs. The synthesis was performed using a standard Schlenk line technique. First, a Se-precursor solution was prepared according to the previously reported method.[31] Briefly, 10 mM of Se powder (0.79 g) was mixed with 5 mL of DDT and 5 mL of OlAm and the mixture was subsequently degassed under vacuum at 60 °C for 1 h. Se powder completely dissolved through the reduction by DDT, forming alkylammonium selenide brown stock solution, which was cooled to room temperature and stored in a nitrogen filled glovebox. In a typical NPLs synthesis procedure, 1 mM of $Cu(acac)_2$ (262 mg) was mixed with 3.5 mL of DDT and 10 mL of OlAm in a three-neck round-bottom flask and the mixture was degassed under vacuum (pressure of $2-5 \times 10^{-2}$ Torr) and vigorous stirring at 60 °C for 1 h. Afterward, the flask was filled with nitrogen and quickly heated to 220 °C (4−5 min to reach the temperature). $Cu(acac)_2$ completely dissolved forming a clear yellow solution. At this temperature a mixture of 0.5 mL of the Se-precursor, prepared as described above, with 1.5 mL of DDT was swiftly injected, using a syringe, into the flask leading to immediate color change from yellow to brown. The reaction mixture was kept at 220 °C for 4 min and then cooled to room temperature. For further characterization, the prepared NPLs were purified in an inert gas atmosphere by centrifugation of the crude reaction mixture with subsequent dissolving of the precipitate in 2−3 mL of chloroform. This solution was washed 2−3 times by adding 1−2 mL of methanol, precipitating NPLs by centrifugation and redissolving them in chloroform. As a byproduct of the synthesis a small fraction (less than 10%) of spherical $Cu_{2-x}Se_yS_{1-y}$ NCs with sizes of approximately 5−6 nm was formed. These particles were easily separated by centrifugation of the reaction mixture, after which they remained in solution whereas the platelets precipitated.

***In situ* Cation Exchange.** For the cation exchange, a crude reaction mixture was used without further purification. Three milliliters of the mixture and 1 mL of TOP were added to a dispersion of various amounts of $ZnCl_2$ or/and $Sn(acac)_2Cl_2$ (see the Results and Discussion part for the ratios of Cu/Zn/Sn) in 4 mL of ODE, which was previously degassed for approximately 30 min. The temperature of the mixture was raised to 100 °C and kept for 20 min. After cooling, the reaction product was purified using the same procedure as for initial $Cu_{2-x}Se_yS_{1-y}$ NPLs.

Cyclic Voltammetry (CV). All electrochemical measurements were performed using a PARSTAT 2273, in a conventional three electrodes cell. A 0.1 M solution of TBAP in acetonitrile, used as an electrolyte, was purged with nitrogen prior to the measurements and in between the measurements to remove any traces of oxygen. Glassy carbon disc electrodes were polished to mirror-like finish using a diamond paste (0.5 μm diameter particles) and thoroughly rinsed with acetone and dichloromethane. The samples for measurements were prepared in a nitrogen filled glovebox. NPLs were deposited onto the electrodes by drop-casting from chloroform solutions with subsequent drying. Potentials were reported *vs* Ag/AgCl in CV and for calculations *vs* NHE.

Transmission Electron Microscopy (TEM). Samples were prepared by dropping diluted NPL colloidal suspensions onto carbon-coated 200 mesh copper and ultrathin carbon-coated 400 mesh gold grids for conventional TEM and HRTEM imaging, respectively, and letting the solvent evaporate. Conventional TEM observations were carried out using a JEOL JEM 1011 microscope equipped with a thermionic gun operating at 100 kV of accelerating voltage. HRTEM, HAADF-STEM and EDS analyses were performed on a JEOL JEM-2200FS microscope equipped with a field emission gun working at 200 kV, a CEOS spherical aberration corrector of the objective lens allowing for a subangstrom spatial resolution of 0.9 Å. The chemical composition of the NPLs was determined in STEM mode, using a Bruker Quantax 400 system with a 60 mm^2 XFlash 6T silicon drift detector. The elemental quantification and the elemental line profile were performed in STEM-EDS mode using a 0.7 nm electron probe wide. For STEM-EDS chemical analyses, NPL solutions were drop-casted onto ultrathin carbon-coated gold grids and the measurements were carried out using an analytical double tilt holder equipped with a low background beryllium tip in order to avoid any interference between the signals coming from the grid/holder and the NPLs.

Scanning Electron Microscopy-Energy Dispersive X-ray Spectroscopy (SEM-EDS). Additional EDS characterization was performed on a high resolution scanning electron microscope Jeol JSM-7500F equipped with a cold field emission gun using an Oxford X-Max 80 system with a silicon drift detector having an 80 mm^2 effective area. The analyses were done with an accelerating voltage of 10 kV, and the spectra were acquired for 300 s live time. Standardless quantification was achieved with Aztec Energy EDS Software.

X-ray Photoelectron Spectroscopy (XPS). The samples were prepared in a glovebox by drop-casting NPL colloids on a graphite substrate (HOPG, ZYB quality, NT-MDT) and then transferred to the XPS setup avoiding air-exposure. Measurements were performed on a Kratos Axis Ultra DLD spectrometer, using a monochromatic Al Kα source (15 kV, 20 mA). Wide scans were acquired at analyzer pass energy of 160 eV. High resolution narrow scans were performed at constant pass energy of 10 eV and steps of 0.05 eV. The photoelectrons were detected at a takeoff angle of $\Phi = 0°$ with respect to the surface normal. The pressure in the analysis chamber was maintained below 7×10^{-9} Torr for data acquisition. The data were converted to VAMAS format and processed using CasaXPS software, version 2.3.15. The binding energy (BE) scale was internally referenced to the C 1s peak (BE for C−C = 284.8 eV).

Powder X-ray Diffraction (XRD). XRD patterns were recorded on a Rigaku SmartLab 9 kW diffractometer. The X-ray source was operated at 40 kV and 150 mA. The diffractometer was equipped with a Cu source and a Göbel mirror to obtain a parallel beam and to suppress Cu Kβ radiation (1.392 Å). To acquire data, a 2-theta/omega scan geometry was used. The samples were prepared by drop casting concentrated NPL solutions onto a zero background silicon substrate. The PDXL software of Rigaku was used for phase identification.

UV−vis−NIR Spectroscopy. Absorbance spectra of NPLs dissolved in TCE were measured in 1 cm path length quartz cuvettes using a Varian Cary 5000 UV−vis−NIR spectrophotometer. Dilute NPL solutions were prepared inside a nitrogen filled glovebox.

Raman Spectroscopy. Raman spectra were recorded using an optical microscope with 50× objective attached to a HR800 (Jobin Yvon) spectrometer with an excitation wavelength of 632 nm. Power incident on the sample surface was about 4 mW with a laser spot size of about 150 μm. Dispersion of the Raman scattering was achieved through a grating with 1800 lines/mm. Data acquisition was done for 120 s in the range of 300−100 cm^{-1}. Colloidal NPLs were drop-cast on a silicon wafer under inert atmosphere.

Elemental Analysis. Inductively coupled plasma optical emission spectroscopy (ICP-OES) analysis performed on an iCAP 6000 spectrometer (ThermoScientific) was used to quantify the copper content in the NPLs. The samples were digested in aqua regia (HCl/HNO_3 = 3/1 (v/v)) prior to measurements.

Conflict of Interest: The authors declare no competing financial interest.

Supporting Information Available: Size distribution histograms of the pristine and exchanged NPLs; TEM image of initial $Cu_{2-x}Se_yS_{1-y}$ NPLs assembling in stripes; Raman spectra of CZTSeS2 and CZTSeS5 NPLs; tables summarizing elemental compositions of the samples, as well as XPS peak positions from Figure 4; absorbance spectra of all compounds obtained, as well as those of CZTSeS5 NPLs before and after addition of the oxidizing agent. This material is available free of charge *via* the Internet at http://pubs.acs.org.

Acknowledgment. V.L. gratefully acknowledges the support by a Marie Curie Intra European Fellowship within the 7th European Community Framework Programme (FP7/2007-2013) under the grant agreement no. 301100 (project "LOTOCON"). The research leading to these results has also received funding from the FP7 under grant agreement nos. 614897 (ERC Consolidator Grant "TRANS-NANO"), and 284486 (project "SCALENANO").

REFERENCES AND NOTES

1. Guo, Q.; Ford, G. M.; Hillhouse, H. W.; Agrawal, R. Sulfide Nanocrystal Inks for Dense $Cu(In_{1-x}Ga_x)(S_{1-y}Se_y)_2$ Absorber Films and Their Photovoltaic Performance. *Nano Lett.* **2009**, *9*, 3060–3065.
2. Guo, Q.; Hillhouse, H. W.; Agrawal, R. Synthesis of Cu_2ZnSnS_4 Nanocrystal Ink and Its Use for Solar Cells. *J. Am. Chem. Soc.* **2009**, *131*, 11672–11673.
3. Guo, Q.; Ford, G. M.; Yang, W.-C.; Walker, B. C.; Stach, E. A.; Hillhouse, H. W.; Agrawal, R. Fabrication of 7.2% Efficient CZTSSe Solar Cells Using CZTS Nanocrystals. *J. Am. Chem. Soc.* **2010**, *132*, 17384–17386.
4. Riha, S. C.; Parkinson, B. A.; Prieto, A. L. Solution-Based Synthesis and Characterization of Cu_2ZnSnS_4 Nanocrystals. *J. Am. Chem. Soc.* **2009**, *131*, 12054–12055.
5. Steinhagen, C.; Panthani, M. G.; Akhavan, V.; Goodfellow, B.; Koo, B.; Korgel, B. A. Synthesis of Cu_2ZnSnS_4 Nanocrystals for Use in Low-Cost Photovoltaics. *J. Am. Chem. Soc.* **2009**, *131*, 12554–12555.
6. Akhavan, V. A.; Goodfellow, B. W.; Panthani, M. G.; Steinhagen, C.; Harvey, T. B.; Stolle, C. J.; Korgel, B. A. Colloidal CIGS and CZTS Nanocrystals: A Precursor Route to Printed Photovoltaics. *J. Solid State Chem.* **2012**, *189*, 2–12.
7. Kim, Y.; Woo, K.; Kim, I.; Cho, Y. S.; Jeong, S.; Moon, J. Highly Concentrated Synthesis of Copper-Zinc-Tin-Sulfide Nanocrystals with Easily Decomposable Capping Molecules for Printed Photovoltaic Applications. *Nanoscale* **2013**, *5*, 10183–10188.

8. Guo, Q.; Kim, S. J.; Kar, M.; Shafarman, W. N.; Birkmire, R. W.; Stach, E. A.; Agrawal, R.; Hillhouse, H. W. Development of $CuInSe_2$ Nanocrystal and Nanoring Inks for Low-Cost Solar Cells. *Nano Lett.* **2008**, *8*, 2982–2987.
9. Cao, Y.; Denny, M. S.; Caspar, J. V.; Farneth, W. E.; Guo, Q.; Ionkin, A. S.; Johnson, L. K.; Lu, M.; Malajovich, I.; Radu, D.; *et al.* High-Efficiency Solution-Processed $Cu_2ZnSn(S,Se)_4$ Thin-Film Solar Cells Prepared from Binary and Ternary Nanoparticles. *J. Am. Chem. Soc.* **2012**, *134*, 15644–15647.
10. Ramasamy, K.; Malik, M. A.; Revaprasadu, N.; O'Brien, P. Routes to Nanostructured Inorganic Materials with Potential for Solar Energy Applications. *Chem. Mater.* **2013**, *25*, 3551–3569.
11. van Embden, J.; Chesman, A. S. R.; Della Gaspera, E.; Duffy, N. W.; Watkins, S. E.; Jasieniak, J. J. $Cu_2ZnSnS_{4x}Se_{4(1-x)}$ Solar Cells from Polar Nanocrystal Inks. *J. Am. Chem. Soc.* **2014**, *136*, 5237–5240.
12. Guo, Q.; Ford, G. M.; Yang, W.-C.; Hages, C. J.; Hillhouse, H. W.; Agrawal, R. Enhancing the Performance of CZTSSe Solar Cells with Ge Alloying. *Sol. Energy Mater. Sol. Cells* **2012**, *105*, 132–136.
13. Zhou, H.; Song, T.-B.; Hsu, W.-C.; Luo, S.; Ye, S.; Duan, H.-S.; Hsu, C.-J.; Yang, W.; Yang, Y. Rational Defect Passivation of $Cu_2ZnSn(S,Se)_4$ Photovoltaics with Solution-Processed Cu_2ZnSnS_4:Na Nanocrystals. *J. Am. Chem. Soc.* **2013**, *135*, 15998–16001.
14. Yang, W.-C.; Miskin, C. K.; Hages, C. J.; Hanley, E. C.; Handwerker, C.; Stach, E. A.; Agrawal, R. Kesterite $Cu_2ZnSn(S,Se)_4$ Absorbers Converted from Metastable, Wurtzite-Derived Cu_2ZnSnS_4 Nanoparticles. *Chem. Mater.* **2014**, *26*, 3530–3534.
15. Liu, M.-L.; Chen, I. W.; Huang, F.-Q.; Chen, L.-D. Improved Thermoelectric Properties of Cu-Doped Quaternary Chalcogenides of $Cu_2CdSnSe_4$. *Adv. Mater.* **2009**, *21*, 3808–3812.
16. Yang, H.; Jauregui, L. A.; Zhang, G.; Chen, Y. P.; Wu, Y. Nontoxic and Abundant Copper Zinc Tin Sulfide Nanocrystals for Potential High-Temperature Thermoelectric Energy Harvesting. *Nano Lett.* **2012**, *12*, 540–545.
17. Ibáñez, M.; Zamani, R.; LaLonde, A.; Cadavid, D.; Li, W.; Shavel, A.; Arbiol, J.; Morante, J. R.; Gorsse, S.; Snyder, G. J.; *et al.* $Cu_2ZnGeSe_4$ Nanocrystals: Synthesis and Thermoelectric Properties. *J. Am. Chem. Soc.* **2012**, *134*, 4060–4063.
18. Ibáñez, M.; Cadavid, D.; Zamani, R.; García-Castelló, N.; Izquierdo-Roca, V.; Li, W.; Fairbrother, A.; Prades, J. D.; Shavel, A.; Arbiol, J.; *et al.* Composition Control and Thermoelectric Properties of Quaternary Chalcogenide Nanocrystals: The Case of Stannite $Cu_2CdSnSe_4$. *Chem. Mater.* **2012**, *24*, 562–570.
19. Ibáñez, M.; Cadavid, D.; Anselmi-Tamburini, U.; Zamani, R.; Gorsse, S.; Li, W.; López, A. M.; Morante, J. R.; Arbiol, J.; Cabot, A. Colloidal Synthesis and Thermoelectric Properties of Cu_2SnSe_3 Nanocrystals. *J. Mater. Chem. A* **2013**, *1*, 1421–1426.
20. Li, W. H.; Ibáñez, M.; Zamani, R. R.; García-Castelló, N.; Gorsse, S.; Cadavid, D.; Prades, J. D.; Arbiol, J.; Cabot, A. $Cu_2HgSnSe_4$ Nanoparticles: Synthesis and Thermoelectric Properties. *CrystEngComm* **2013**, *15*, 8966–8971.
21. Ibáñez, M.; Zamani, R.; Li, W.; Cadavid, D.; Gorsse, S.; Katcho, N. A.; Shavel, A.; López, A. M.; Morante, J. R.; Arbiol, J.; *et al.* Crystallographic Control at the Nanoscale To Enhance Functionality: Polytypic Cu_2GeSe_3 Nanoparticles as Thermoelectric Materials. *Chem. Mater.* **2012**, *24*, 4615–4622.
22. Chen, S.; Gong, X. G.; Walsh, A.; Wei, S.-H. Crystal and Electronic Band Structure of Cu_2ZnSnX_4 (X=S and Se) Photovoltaic Absorbers: First-Principles Insights. *Appl. Phys. Lett.* **2009**, *94*, 041903.
23. Singh, A.; Singh, S.; Levcenko, S.; Unold, T.; Laffir, F.; Ryan, K. M. Compositionally Tunable Photoluminescence Emission in $Cu_2ZnSn(S_{1-x}Se_x)_4$ Nanocrystals. *Angew. Chem., Int. Ed.* **2013**, *52*, 9120–9124.
24. Chesman, A. S. R.; Duffy, N. W.; Peacock, S.; Waddington, L.; Webster, N. A. S.; Jasieniak, J. J. Non-Injection Synthesis of Cu_2ZnSnS_4 Nanocrystals Using a Binary Precursor and Ligand Approach. *RSC Adv.* **2013**, *3*, 1017–1020.
25. Chesman, A. S. R.; van Embden, J.; Duffy, N. W.; Webster, N. A. S.; Jasieniak, J. J. *In Situ* Formation of Reactive Sulfide Precursors in the One-Pot, Multigram Synthesis of Cu_2ZnSnS_4 Nanocrystals. *Cryst. Growth Des.* **2013**, *13*, 1712–1720.
26. Shavel, A.; Cadavid, D.; Ibáñez, M.; Carrete, A.; Cabot, A. Continuous Production of Cu_2ZnSnS_4 Nanocrystals in a Flow Reactor. *J. Am. Chem. Soc.* **2012**, *134*, 1438–1441.
27. Singh, A.; Geaney, H.; Laffir, F.; Ryan, K. M. Colloidal Synthesis of Wurtzite Cu_2ZnSnS_4 Nanorods and Their Perpendicular Assembly. *J. Am. Chem. Soc.* **2012**, *134*, 2910–2913.
28. Peng, Q.; Lu, X. T.; Zhuang, Z. B.; Li, Y. D. Wurtzite Cu_2ZnSnS_4 Nanocrystals: A Novel Quaternary Semiconductor. *Chem. Commun.* **2011**, *47*, 3141–3143.
29. Shavel, A.; Arbiol, J.; Cabot, A. Synthesis of Quaternary Chalcogenide Nanocrystals: Stannite $Cu_2Zn_xSn_ySe_{1+x+2y}$. *J. Am. Chem. Soc.* **2010**, *132*, 4514–4515.
30. Haas, W.; Rath, T.; Pein, A.; Rattenberger, J.; Trimmel, G.; Hofer, F. The Stoichiometry of Single Nanoparticles of Copper Zinc Tin Selenide. *Chem. Commun.* **2011**, *47*, 2050–2052.
31. Liu, Y.; Yao, D.; Shen, L.; Zhang, H.; Zhang, X.; Yang, B. Alkylthiol-Enabled Se Powder Dissolution in Oleylamine at Room Temperature for the Phosphine-Free Synthesis of Copper-Based Quaternary Selenide Nanocrystals. *J. Am. Chem. Soc.* **2012**, *134*, 7207–7210.
32. Jiang, C.; Lee, J.-S.; Talapin, D. V. Soluble Precursors for $CuInSe_2$, $CuIn_{1-x}Ga_xSe_2$, and $Cu_2ZnSn(S,Se)_4$ Based on Colloidal Nanocrystals and Molecular Metal Chalcogenide Surface Ligands. *J. Am. Chem. Soc.* **2012**, *134*, 5010–5013.
33. Lin, X.; Kavalakkatt, J.; Kornhuber, K.; Abou-Ras, D.; Schorr, S.; Lux-Steiner, M. C.; Ennaoui, A. Synthesis of $Cu_2Zn_xSn_ySe_{1+x+2y}$ Nanocrystals with Wurtzite-Derived Structure. *RSC Adv.* **2012**, *2*, 9894–9898.
34. Son, D. H.; Hughes, S. M.; Yin, Y.; Alivisatos, A. P. Cation Exchange Reactions in Ionic Nanocrystals. *Science* **2004**, *306*, 1009–1012.
35. Robinson, R. D.; Sadtler, B.; Demchenko, D. O.; Erdonmez, C. K.; Wang, L.-W.; Alivisatos, A. P. Spontaneous Superlattice Formation in Nanorods through Partial Cation Exchange. *Science* **2007**, *317*, 355–358.
36. Jain, P. K.; Amirav, L.; Aloni, S.; Alivisatos, A. P. Nanoheterostructure Cation Exchange: Anionic Framework Conservation. *J. Am. Chem. Soc.* **2010**, *132*, 9997–9999.
37. Luther, J. M.; Zheng, H.; Sadtler, B.; Alivisatos, A. P. Synthesis of PbS Nanorods and Other Ionic Nanocrystals of Complex Morphology by Sequential Cation Exchange Reactions. *J. Am. Chem. Soc.* **2009**, *131*, 16851–16857.
38. Beberwyck, B. J.; Surendranath, Y.; Alivisatos, A. P. Cation Exchange: A Versatile Tool for Nanomaterials Synthesis. *J. Phys. Chem. C* **2013**, *117*, 19759–19770.
39. Beberwyck, B. J.; Alivisatos, A. P. Ion Exchange Synthesis of III-V Nanocrystals. *J. Am. Chem. Soc.* **2012**, *134*, 19977–19980.
40. Rivest, J. B.; Jain, P. K. Cation Exchange on the Nanoscale: An Emerging Technique for New Material Synthesis, Device Fabrication, and Chemical Sensing. *Chem. Soc. Rev.* **2013**, *42*, 89–96.
41. Bouet, C.; Tessier, M. D.; Ithurria, S.; Mahler, B.; Nadal, B.; Dubertret, B. Flat Colloidal Semiconductor Nanoplatelets. *Chem. Mater.* **2013**, *25*, 1262–1271.
42. Choi, J.; Kang, N.; Yang, H. Y.; Kim, H. J.; Son, S. U. Colloidal Synthesis of Cubic-Phase Copper Selenide Nanodiscs and Their Optoelectronic Properties. *Chem. Mater.* **2010**, *22*, 3586–3588.
43. Du, W.; Qian, X.; Ma, X.; Gong, Q.; Cao, H.; Yin, J. Shape-Controlled Synthesis and Self-Assembly of Hexagonal Covellite (CuS) Nanoplatelets. *Chem.—Eur. J.* **2007**, *13*, 3241–3247.
44. Zhuang, Z.; Peng, Q.; Zhang, B.; Li, Y. Controllable Synthesis of Cu_2S Nanocrystals and their Assembly into a Superlattice. *J. Am. Chem. Soc.* **2008**, *130*, 10482–10483.
45. Du, X.-S.; Yu, Z.-Z.; Dasari, A.; Ma, J.; Meng, Y.-Z.; Mai, Y.-W. Facile Synthesis and Assembly of Cu_2S Nanodisks to

Corncoblike Nanostructures. *Chem. Mater.* **2006**, *18*, 5156–5158.

46. Saunders, A. E.; Ghezelbash, A.; Smilgies, D. M.; Sigman, M. B., Jr.; Korgel, B. A. Columnar Self-Assembly of Colloidal Nanodisks. *Nano Lett.* **2006**, *6*, 2959–2963.
47. Saldanha, P. L.; Brescia, R.; Prato, M.; Li, H.; Povia, M.; Manna, L.; Lesnyak, V. Generalized One-Pot Synthesis of Copper Sulfide, Selenide-Sulfide, and Telluride-Sulfide Nanoparticles. *Chem. Mater.* **2014**, *26*, 1442–1449.
48. Li, H.; Brescia, R.; Povia, M.; Prato, M.; Bertoni, G.; Manna, L.; Moreels, I. Synthesis of Uniform Disk-Shaped Copper Telluride Nanocrystals and Cation Exchange to Cadmium Telluride Quantum Disks with Stable Red Emission. *J. Am. Chem. Soc.* **2013**, *135*, 12270–12278.
49. Li, H.; Zanella, M.; Genovese, A.; Povia, M.; Falqui, A.; Giannini, C.; Manna, L. Sequential Cation Exchange in Nanocrystals: Preservation of Crystal Phase and Formation of Metastable Phases. *Nano Lett.* **2011**, *11*, 4964–4970.
50. Li, H.; Brescia, R.; Krahne, R.; Bertoni, G.; Alcocer, M. J. P.; D'Andrea, C.; Scotognella, F.; Tassone, F.; Zanella, M.; De Giorgi, M.; *et al.* Blue-UV-Emitting ZnSe(Dot)/ZnS(Rod) Core/Shell Nanocrystals Prepared from CdSe/CdS Nanocrystals by Sequential Cation Exchange. *ACS Nano* **2012**, *6*, 1637–1647.
51. Lide, D. R. *CRC Handbook of Chemistry and Physics*, 84th ed.; CRC Press: Boca Raton, FL, 2003−2004.
52. Norako, M. E.; Greaney, M. J.; Brutchey, R. L. Synthesis and Characterization of Wurtzite-Phase Copper Tin Selenide Nanocrystals. *J. Am. Chem. Soc.* **2012**, *134*, 23–26.
53. Ishii, M.; Shibata, K.; Nozaki, H. Anion Distributions and Phase Transitions in $\mathrm{CuS_{1-x}Se_x}(x = 0-1)$ Studied by Raman Spectroscopy. *J. Solid State Chem.* **1993**, *105*, 504–511.
54. Marcano, G.; Rincón, C.; López, S. A.; Sánchez Pérez, G.; Herrera-Pérez, J. L.; Mendoza-Alvarez, J. G.; Rodríguez, P. Raman Spectrum of Monoclinic Semiconductor. *Solid State Commun.* **2011**, *151*, 84–86.
55. Taylor, W. The Raman Spectra of Cubic Zinc Selenide and Telluride. *Phys. Lett. A* **1967**, *24*, 556–558.
56. Cheng, Y. C.; Jin, C. Q.; Gao, F.; Wu, X. L.; Zhong, W.; Li, S. H.; Chu, P. K. Raman Scattering Study of Zinc Blende and Wurtzite ZnS. *J. Appl. Phys.* **2009**, *106*, 123505.
57. Riha, S. C.; Johnson, D. C.; Prieto, A. L. $\mathrm{Cu_2Se}$ Nanoparticles with Tunable Electronic Properties Due to a Controlled Solid-State Phase Transition Driven by Copper Oxidation and Cationic Conduction. *J. Am. Chem. Soc.* **2011**, *133*, 1383–1390.
58. Naumkin, A. V.; Kraut-Vass, A.; Gaarenstroom, S. W.; Powell, C. J. *NIST X-ray Photoelectron Spectroscopy Database*, Version 4.1; National Institute of Standards and Technology: Gaithersburg, **2012**. http://srdata.nist.gov/xps/.
59. Zhao, Y.; Pan, H.; Lou, Y.; Qiu, X.; Zhu, J.; Burda, C. Plasmonic $\mathrm{Cu_{2-x}S}$ Nanocrystals: Optical and Structural Properties of Copper-Deficient Copper(I) Sulfides. *J. Am. Chem. Soc.* **2009**, *131*, 4253–4261.
60. Luther, J. M.; Jain, P. K.; Ewers, T.; Alivisatos, A. P. Localized Surface Plasmon Resonances Arising from Free Carriers in Doped Quantum Dots. *Nat. Mater.* **2011**, *10*, 361–366.
61. Comin, A.; Manna, L. New Materials for Tunable Plasmonic Colloidal Nanocrystals. *Chem. Soc. Rev.* **2014**, *43*, 3957–3975.
62. Dorfs, D.; Härtling, T.; Miszta, K.; Bigall, N. C.; Kim, M. R.; Genovese, A.; Falqui, A.; Povia, M.; Manna, L. Reversible Tunability of the Near-Infrared Valence Band Plasmon Resonance in $\mathrm{Cu_{2-x}Se}$ Nanocrystals. *J. Am. Chem. Soc.* **2011**, *133*, 11175–11180.
63. Dilena, E.; Dorfs, D.; George, C.; Miszta, K.; Povia, M.; Genovese, A.; Casu, A.; Prato, M.; Manna, L. Colloidal $\mathrm{Cu_{2-x}(S_ySe_{1-y})}$ Alloy Nanocrystals with Controllable Crystal Phase: Synthesis, Plasmonic Properties, Cation Exchange and Electrochemical Lithiation. *J. Mater. Chem.* **2012**, *22*, 13023–13031.
64. Kriegel, I.; Jiang, C.; Rodríguez-Fernández, J.; Schaller, R. D.; Talapin, D. V.; da Como, E.; Feldmann, J. Tuning the Excitonic and Plasmonic Properties of Copper Chalcogenide Nanocrystals. *J. Am. Chem. Soc.* **2012**, *134*, 1583–1590.
65. Liu, X.; Wang, X.; Zhou, B.; Law, W.-C.; Cartwright, A. N.; Swihart, M. T. Size-Controlled Synthesis of $\mathrm{Cu_{2-x}E}$ (E = S, Se) Nanocrystals with Strong Tunable Near-Infrared Localized Surface Plasmon Resonance and High Conductivity in Thin Films. *Adv. Funct. Mater.* **2013**, *23*, 1256–1264.
66. Liu, X.; Wang, X.; Swihart, M. T. $\mathrm{Cu_{2-x}S_{1-y}Se_y}$ Alloy Nanocrystals with Broadly Tunable Near-Infrared Localized Surface Plasmon Resonance. *Chem. Mater.* **2013**, *25*, 4402–4408.
67. Xie, Y.; Carbone, L.; Nobile, C.; Grillo, V.; D'Agostino, S.; Della Sala, F.; Giannini, C.; Altamura, D.; Oelsner, C.; Kryschi, C.; *et al.* Metallic-like Stoichiometric Copper Sulfide Nanocrystals: Phase- and Shape-Selective Synthesis, Near-Infrared Surface Plasmon Resonance Properties, and Their Modeling. *ACS Nano* **2013**, *7*, 7352–7369.
68. Xie, Y.; Riedinger, A.; Prato, M.; Casu, A.; Genovese, A.; Guardia, P.; Sottini, S.; Sangregorio, C.; Miszta, K.; Ghosh, S.; *et al.* Copper Sulfide Nanocrystals with Tunable Composition by Reduction of Covellite Nanocrystals with $\mathrm{Cu^+}$ Ions. *J. Am. Chem. Soc.* **2013**, *135*, 17630–17637.
69. Tian, Q.; Xu, X.; Han, L.; Tang, M.; Zou, R.; Chen, Z.; Yu, M.; Yang, J.; Hu, J. Hydrophilic $\mathrm{Cu_2ZnSnS_4}$ Nanocrystals for Printing Flexible, Low-Cost and Environmentally Friendly Solar Cells. *CrystEngComm* **2012**, *14*, 3847–3850.
70. Johansson, T.; Mammo, W.; Svensson, M.; Andersson, M. R.; Inganas, O. Electrochemical Bandgaps of Substituted Polythiophenes. *J. Mater. Chem.* **2003**, *13*, 1316–1323.
71. Bredas, J. L.; Silbey, R.; Boudreaux, D. S.; Chance, R. R. Chain-Length Dependence of Electronic and Electrochemical Properties of Conjugated Systems: Polyacetylene, Polyphenylene, Polythiophene, and Polypyrrole. *J. Am. Chem. Soc.* **1983**, *105*, 6555–6559.
72. Amelia, M.; Lincheneau, C.; Silvi, S.; Credi, A. Electrochemical Properties of CdSe and CdTe Quantum Dots. *Chem. Soc. Rev.* **2012**, *41*, 5728–5743.
73. Li, Y. C.; Zhong, H. Z.; Li, R.; Zhou, Y.; Yang, C. H.; Li, Y. F. High-Yield Fabrication and Electrochemical Characterization of Tetrapodal CdSe, CdTe, and $\mathrm{CdSe_xTe_{1-x}}$ Nanocrystals. *Adv. Funct. Mater.* **2006**, *16*, 1705–1716.
74. Ingole, P. P.; Markad, G. B.; Saraf, D.; Tatikondewar, L.; Nene, O.; Kshirsagar, A.; Haram, S. K. Band Gap Bowing at Nanoscale: Investigation of $\mathrm{CdS_xSe_{1-x}}$ Alloy Quantum Dots through Cyclic Voltammetry and Density Functional Theory. *J. Phys. Chem. C* **2013**, *117*, 7376–7383.
75. Ahmadi, M.; Pramana, S. S.; Batabyal, S. K.; Boothroyd, C.; Mhaisalkar, S. G.; Lam, Y. M. Synthesis of $\mathrm{Cu_2SnSe_3}$ Nanocrystals for Solution Processable Photovoltaic Cells. *Inorg. Chem.* **2013**, *52*, 1722–1728.
76. Zhong, H.; Lo, S. S.; Mirkovic, T.; Li, Y.; Ding, Y.; Li, Y.; Scholes, G. D. Noninjection Gram-Scale Synthesis of Monodisperse Pyramidal $\mathrm{CuInS_2}$ Nanocrystals and Their Size-Dependent Properties. *ACS Nano* **2010**, *4*, 5253–5262.
77. Haram, S. K.; Quinn, B. M.; Bard, A. J. Electrochemistry of CdS Nanoparticles: A Correlation between Optical and Electrochemical Band Gaps. *J. Am. Chem. Soc.* **2001**, *123*, 8860–8861.
78. Wang, J.-J.; Xue, D.-J.; Guo, Y.-G.; Hu, J.-S.; Wan, L.-J. Bandgap Engineering of Monodispersed $\mathrm{Cu_{2-x}S_ySe_{1-y}}$ Nanocrystals through Chalcogen Ratio and Crystal Structure. *J. Am. Chem. Soc.* **2011**, *133*, 18558–18561.
79. Meyer, B.; Zhang, S.; Scholz, F. The Quantitative Analysis of Mixed Crystals $\mathrm{CuS_xSe_{1-x}}$ with Abrasive Stripping Voltammetry and a Redetermination of the Solubility Product of CuSe and the Standard Potential of the Cu/CuSe Electrode. *Fresenius J. Anal. Chem.* **1996**, *356*, 267–270.
80. Grätzel, M. Photoelectrochemical Cells. *Nature* **2001**, *414*, 338–344.
81. Pattantyus-Abraham, A. G.; Kramer, I. J.; Barkhouse, A. R.; Wang, X.; Konstantatos, G.; Debnath, R.; Levina, L.; Raabe, I.; Nazeeruddin, M. K.; Grätzel, M.; *et al.* Depleted-Heterojunction Colloidal Quantum Dot Solar Cells. *ACS Nano* **2010**, *4*, 3374–3380.
82. Barkhouse, D. A. R.; Debnath, R.; Kramer, I. J.; Zhitomirsky, D.; Pattantyus-Abraham, A. G.; Levina, L.; Etgar, L.; Grätzel, M.; Sargent, E. H. Depleted Bulk Heterojunction Colloidal

Quantum Dot Photovoltaics. *Adv. Mater.* **2011**, *23*, 3134–3138.

83. Tang, J.; Sargent, E. H. Infrared Colloidal Quantum Dots for Photovoltaics: Fundamentals and Recent Progress. *Adv. Mater.* **2011**, *23*, 12–29.
84. Chen, G.; Seo, J.; Yang, C.; Prasad, P. N. Nanochemistry and Nanomaterials for Photovoltaics. *Chem. Soc. Rev.* **2013**, *42*, 8304–8338.
85. Kamat, P. V. Quantum Dot Solar Cells. The Next Big Thing in Photovoltaics. *J. Phys. Chem. Lett.* **2013**, *4*, 908–918.
86. Ma, X.; Mews, A.; Kipp, T. Determination of Electronic Energy Levels in Type-II CdTe-Core/CdSe-Shell and CdSe-Core/CdTe-Shell Nanocrystals by Cyclic Voltammetry and Optical Spectroscopy. *J. Phys. Chem. C* **2013**, *117*, 16698–16708.
87. Ji, S.; Shi, T.; Qiu, X.; Zhang, J.; Xu, G.; Chen, C.; Jiang, Z.; Ye, C. A Route to Phase Controllable $Cu_2ZnSn(S_{1-x}Se_x)_4$ Nanocrystals with Tunable Energy Bands. *Sci. Rep.* **2013**, *3*, No. 2733.